Photocatalytic behaviour of nanocarbon-TiO_2 composites and immobilization into hollow fibres

Luisa M. Pastrana-Martínez[a], Sergio Morales-Torres[a], Sergios K. Papageorgiou[b,*], Fotis K. Katsaros[b], George E. Romanos[b], José L. Figueiredo[a], Joaquim L. Faria[a], Polycarpos Falaras[b], Adrián M.T. Silva[a,*]

[a] *LCM – Laboratory of Catalysis and Materials – Associate Laboratory LSRE/LCM, Faculdade de Engenharia, Universidade do Porto, Rua Dr. Roberto Frias, 4200-465 Porto, Portugal; Fax: +351-22-5081449; Tel: +351-22-5081582.*

[b] *Division of Physical Chemistry, Institute of Advanced Materials, Physicochemical Processes, Nanotechnology and Microsystems (IAMPPNM), National Center for Scientific Research "Demokritos", 153 10 Aghia Paraskevi Attikis, Athens, Greece*

*Corresponding authors e-mail addresses:

adrian@fe.up.pt (A.M.T. Silva)

spap@chem.demokritos.gr (S.K. Papageorgiou)

Abstract

Nanocarbon-TiO_2 composites were prepared by the liquid phase deposition method using TiO_2 and three different nanocarbon materials: carbon nanotubes, fullerenes and graphene oxide. The photocatalytic efficiency of these composites was studied for the degradation of diphenhydramine pharmaceutical and methyl orange azo-dye compounds. The results suggest different synergistic effects between the carbon phase and the TiO_2 particles depending on the nature and content of the nanocarbon material employed. Among all the materials tested, the titania composite containing 4 wt.% of graphene oxide exhibited the highest photocatalytic activity under both near-UV/Vis and visible light irradiation, outperforming the synthesized bare TiO_2 and the benchmark Evonik P25 TiO_2 photocatalyst. The high efficiency of the composite containing graphene oxide was attributed to the optimal assembly between the TiO_2 nanoparticles and graphene oxide sheets, making the material to act simultaneously as electron acceptor and donor, thus supressing charge recombination. Aiming at technological applications, this photocatalyst was immobilized into hollow fibres, showing significant catalytic activity and stability in continuous operation.

Keywords*: photocatalysis; carbon nanotubes; fullerenes; graphene oxide; hollow fibres.*

1. Introduction

Nanocarbon materials such as carbon nanotubes (CNT), fullerenes (C_{60}) and graphene oxide (GO) offer the benefit of their special structural and electronic properties to develop effective semiconductor photocatalysts when combined with titanium dioxide (TiO_2) [1-3]. CNT-TiO_2 composites have been already tested for the photocatalytic degradation of many different pollutants, including phenol [4-6], phenolic derivatives (e.g., chlorophenol, nitrophenol and aminophenol [7]), benzene derivatives (e.g., aniline, nitrobenzene and benzoic acid [8]) and azo dyes (e.g., methylene blue [9-11] and rhodamine B [12]). For instance, Wang et al. [4] observed a synergistic effect on the phenol removal under UV and visible light irradiation when CNT (20% weight ratio) were combined with TiO_2. Yao et al. [6] also found a beneficial effect for the photocatalytic oxidation of phenol when single- and multi-walled CNT where combined with anatase TiO_2. Gao et al [9] reported the synthesis of CNT-TiO_2 composites by a novel surfactant wrapping sol–gel method for methylene blue degradation. The addition of CNT enhanced the photocatalytic efficiency of TiO_2 in all these studies, but in some particular cases the same (or even lower) photocatalytic activity is observed when CNT are combined with TiO_2, especially when molecules containing strong electron-withdrawing (deactivating) groups are targeted as model pollutants [7].

The combination of C_{60} and TiO_2 is much less studied in photocatalysis, although the activity of C_{60}-TiO_2 composites has been successfully reported for the photocatalytic reduction of Cr(VI) ions [13] and for the degradation of some azo dyes (e.g., rhodamine B [14], methylene blue [15] and procion red [16]). Krishna et al. [16] explored the efficiency of water soluble polyhydroxy fullerenes (PHFs) to enhance the TiO_2 photocatalytic process. The enhanced degradation of procion red under UV conditions, by a factor near to 1.7 in comparison to anatase TiO_2, was justified by the C_{60} acceptance of electrons. This was also suggested in a subsequent study focused on the inactivation of *E. coli* [17]. Long et al. [14] reported that C_{60}

incorporated-TiO_2 nanorods, prepared by a hydrothermal route, presented higher activity for rhodamine blue degradation than pure TiO_2 nanorods and P25 (by factors of 3.3 and 2.7, respectively). More recently, graphene based composites prepared with TiO_2 have attracted a lot of attention for photocatalysis, due to the unique properties of graphene and its derivatives (including GO). Results reported in literature (collected in a recent review [3]) indicate that these composites have been mainly tested for degradation of azo dyes, exhibiting high photocatalytic activity. Zhang et al. [18] prepared GO-P25 composites by a hydrothermal method for photodegradation of methylene blue. Their photocatalytic activity was higher than that obtained with TiO_2 alone or even with CNT-TiO_2 composites with the same carbon content. Akhavan et al. [19] prepared a GO-TiO_2 composite by a sol-gel technique, which allowed a higher photoinactivation of *E. coli* (ca. 7.5 times) than bare anatase TiO_2. GO-P25 composites, prepared by a simple method of mixing and sonication, were also tested in the photodegradation of a commonly employed dye, methyl orange (MO), the best performing photocatalyst being that containing 1.4 wt.% GO and treated at 200-300 ºC [20]. The improved performance was attributed to the reduction of GO during the thermal treatment and to the good contact between TiO_2 and the carbon phase**.** GO-TiO_2 composites are also highly active photocatalysts for degradation of diphenhydramine (DP), an important pharmaceutical pollutant [21, 22].

To further elucidate the key role of the carbon phase on the optimization of the photocatalytic properties, the present work focuses on a series of TiO_2 nanocomposites with relevant carbon materials including CNT, C_{60} and GO. Composites corresponding to two different carbon contents (4 wt.% and 12 wt.%) were synthesized by the liquid phase deposition method [21] and tested (for the degradation of model water pollutants) in photocatalytic experiments under both near-UV/Vis and visible light irradiation, and in the form of powder slurries. Looking towards technological applications, as never tried before, we used a matrix of

alginate porous hollow fibres to immobilize the most active composite and to test its photocatalytic performance.

2. Experimental

2.1. Chemicals

Ammonium hexaflurorotitanate (IV), $(NH_4)_2TiF_6$ (> 99.99%), boric acid, H_3BO_3 (> 99%), ammonium persulfate, $(NH_4)_2S_2O_8$ (> 98%), sulphuric acid, H_2SO_4 (>95%), sodium alginate, (medium viscosity from *macrocystis pyrifera*), high-purity analytical grade DP (99%) and MO (99%) were obtained from Sigma-Aldrich.

2.2. Synthesis of GO and chemical oxidation of CNT and C_{60}

Natural graphite (99.9995% purity from Sigma-Aldrich) was used as precursor of GO. First, graphite oxide was prepared through the modified Hummers method [21, 23]. Then, the resulting material was dispersed in a given volume of water and sonicated with an ultrasonic processor (UP400S, 24 kHz) for 1 h. The resulting sonicated dispersion was centrifuged for 20 min at 3000 r.p.m. to obtain a suspension of GO.

Pristine multi-walled carbon nanotubes (CNT > 95% purity) were purchased from Shenzhen Nanotechnologies Co. Ltd. and fullerenes (C_{60} powder of 99.9% purity) from Materials and Electrochemical Research MER Co. Ltd. Both materials were oxidized with a saturated solution of $(NH_4)_2S_2O_8$ in 1 mol L^{-1} H_2SO_4, as described elsewhere [24]. This oxidizing treatment was different from that used in the preparation of GO, because the use of concentrated H_2SO_4 and $KMnO_4$ (agents used in the modified Hummers method) partially destroys the typical structure of the CNT and C_{60}.

2.3. Preparation of nanocarbon-TiO_2 composites

Different amounts of oxidized CNT and C_{60} were dispersed in distilled water and sonicated for 30 min to obtain a homogeneous suspension similar to that prepared for GO. Then, nanocarbon-TiO_2 composites were synthesized with these dispersions by the liquid phase deposition method (LPD) at room temperature, as described elsewhere for GO [21]. Briefly, ammonium hexafluorotitanate (IV), NH_4TiF_6 (0.1 mol L^{-1}), and boric acid, H_3BO_3 (0.3 mol L^{-1}), were added to different amounts of the nanocarbon dispersions heated at 60 ºC for 2 h under vigorous stirring. The material was separated by filtration, washed with water and dried at 100 ºC under vacuum for 2 h. The post-treatment under N_2 atmosphere at 200 ºC was established in previous experiments, taking into account the crystallinity of TiO_2 particles and the stability of the nanocarbon materials at that temperature. The photocatalysts are denoted as CNT-TiO_2-X, C_{60}-TiO_2-X and GO-TiO_2-X, where X refers to the carbon content used (4 wt.% or 12 wt.%). The carbon loadings were selected taking into account the best (4 wt.%) and the worst (12 wt.%) photocatalytic activity obtained with GO-TiO_2 in our previous work [21]. Bare TiO_2 was also prepared and treated by the same method, without the addition of any carbon material (TiO_2). Degussa P25 from Evonik was used as reference material.

2.4. Preparation of GO-TiO_2 fibres

The composite presenting the highest photocatalytic activity was immobilized into polymer-composite fibres by a similar methodology to that described elsewhere [25]. Briefly, the composite was added to an aqueous solution of sodium alginate under dynamic stirring. When the homogenization was complete, alginate fibres (containing the composite) were prepared by a dry/wet spinning process. The resulting hydrogel hollow fibres were converted to alcogel via successive immersion in a series of ethanol–water solutions of increasing

alcohol concentration (10%, 30%, 50%, 70%, 90%, and 100%) for 1 h, for complete solvent exchange, and the alcohol was evaporated under air at room temperature.

2.5. Characterization techniques

Thermogravimetric (TG) and differential thermogravimetric (DTG) analysis of the composites were performed using a STA 490 PC/4/H Luxx Netzsch thermal analyser, by heating the sample in air flow from 50 ºC to 1000 ºC at 20 ºC min^{-1}. Textural characterization of the samples was carried out by N_2 adsorption-desorption at -196 °C with a Quantachrome NOVA 4200e apparatus. The apparent surface area (S_{BET}) was determined by applying the Brunauer–Emmett-Teller (BET) equation [26]. The volume of nitrogen adsorbed at a relative pressure of 0.95 (V_p), was also obtained from the adsorption isotherms, which corresponds to the sum of the micro- and mesopore volumes according to Gurvitch's rule [27].

The morphology of the composites was determined by scanning electron microscopy (SEM) in a FEI Quanta 400FEG ESEM/EDAX Genesis X4M instrument. The morphology of the hollow fibres was determined by a Jeol JSM 7401F Field Emission Scanning Electron Microscope equipped with Gentle Beam mode. Transmission electron microscopy (TEM) observations were performed on a JEOL JEM-2100, operating at 200 kV and selected-area electron diffraction (SAED) analysis was performed on several zones in order to identify the crystalline structure of TiO_2. The optical properties of the samples were analyzed by UV/Vis diffuse reflectance spectroscopy using a JASCO V-560 UV/Vis spectrophotometer, equipped with an integrating sphere attachment (JASCO ISV-469) and using barium sulfate as reference. The reflectance spectra were converted by the instrument software (JASCO) to equivalent absorption Kubelka-Munk units.

The surface chemistry of the nanocarbon materials was characterized by temperature programmed desorption (TPD) as described elsewhere [28, 29]. The point zero of charge

(pH_{PZC}) of the materials was determined following a pH drift test described elsewhere [30, 31]. First, nitrogen was bubbled in distillate water with the aim to prevent carbon dioxide dissolution and respective water acidification. Then, solutions with varying initial pH (2-12) were prepared using HCl (0.1 mol L^{-1}) or NaOH (0.1 mol L^{-1}) and 50 mL of NaCl (0.01 mol L^{-1}) as electrolyte. Each solution was contacted with 0.15 g of the material and the final pH was measured after 24 h of continuous stirring at room temperature. The PZC value of the material was determined by intercepting the obtained final-pH *vs.* initial-pH curve with the straight line final-pH = initial-pH.

2.6. Photocatalytic experiments

The photocatalytic efficiencies of the nanocarbon catalysts were evaluated for the degradation of 100 mg L^{-1} (3.40×10^{-4} mol L^{-1}) DP and 10 mg L^{-1} (3.05×10^{-5} mol L^{-1}) MO at room temperature (25 ºC) under near-UV/Vis and visible light irradiation. A Heraeus TQ 150 medium-pressure mercury vapour lamp (λ_{exc} = 254, 313, 366, 436 and 546 nm) was held in a quartz immersion tube located inside a DURAN® glass water cooling jacket that was used to control the operating temperature (25 ºC), resulting in near-UV/Vis irradiation (λ > 350 nm). For visible light experiments a cut-off long pass filter was used (λ > 430 nm). The photon flow entering the reactor was ca. 50 mW cm^{-2} or 6 mW cm^{-2}, for near-UV/Vis and visible light irradiation, respectively. These batch experiments were performed in a quartz cylindrical reactor filled with 7.5 mL of solution containing the model pollutant. The suspension was magnetically stirred and continuously purged with an oxygen flow. The load of catalyst was established in preliminary photocatalytic experiments and, in order to avoid an excess of ineffective catalyst, the load was kept at the optimal value of 1.0 g L^{-1} or 0.5 g L^{-1}, for DP and MO, respectively. Samples taken from the reaction mixture were centrifuged to separate the catalyst particles before analysis.

Prior to irradiation, the suspension was magnetically stirred in absence of irradiation (dark phase) to establish the period of time needed to achieve the adsorption-desorption equilibrium of all the nanocarbon catalysts. After equilibration, the concentration of the substrate was measured and taken as the initial concentration (C_0) to discount the adsorption contribution in the dark phase and to determine $t = 0$ for the photocatalytic reactions. Reaction in the absence of catalyst was performed as a blank experiment in order to characterize direct photolysis. The concentration of DP was determined by HPLC with a Hitachi Elite LaChrom system equipped with a Hydrosphere C18 column. The concentration of MO was determined by UV-Vis spectrophotometry at 464 nm in a Jasco V-560 spectrophotometer. The total organic carbon (TOC) was also determined for selected samples using a Shimadzu TOC-5000A analyzer.

The experiments performed with the photocatalyst immobilized into the fibres used the same radiation source, photoreactor and analytical techniques, as mentioned above, only in this case a peristaltic pump was used to continuously supply the DP aqueous solution to the photoreactor. Different operating conditions were previously studied in order to select an adequate residence time in the reactor, namely the flow rate was set at 0.15 mL min^{-1}, the initial concentration of DP at 10 mg L^{-1}, while the load of fibres was determined keeping the amount of TiO_2 at the value used in batch experiments (1.0 g L^{-1}), i.e. taking into account the composite content in these fibres (56 wt.%).

It was found that the photocatalytic oxidation of the studied pollutants in batch experiments can be described by a pseudo-first order kinetic model, according to the following equation:

$$C = C_0 e^{-k t} \qquad (1)$$

where C corresponds to pollutant concentration, k is the pseudo-first order kinetic constant, t is the reaction time and C_0 is the pollutant concentration at $t = 0$. The values of k were

obtained by non-linear regression using the Marquardt–Levenberg algorithm (SigmaPlot software).

3. Results and discussion

3.1. Materials characterization

3.1.1. Thermogravimetric (TG) and differential thermogravimetric (DTG) analysis

The samples were analyzed by TG and DTG analysis (not shown). The carbon content (wt.%) in all composites was determined from the respective weight loss and subtracting the weight loss of neat TiO_2. The obtained results are in a good agreement with the expected carbon content, taking into account that there is no appreciable gasification of any carbon phase during the thermal treatment below 200ºC.

3.1.2. Nitrogen adsorption-desorption isotherms

Table 1 summarizes the determined BET surface area (S_{BET}) and total pore volume (V_p) of the materials. Representative N_2 adsorption-desorption isotherms, for bare TiO_2 and for composites containing 12 wt.% of carbon material, are shown in Figure 1. GO has the lowest S_{BET} (21 m^2 g^{-1}) and V_p (0.027 cm^3 g^{-1}) due to agglomeration of the GO sheets when the suspension is dried to perform the N_2 adsorption analysis [21]. TiO_2 has higher S_{BET} (120 m^2 g^{-1}) and a slightly lower V_p (0.11 cm^3 g^{-1}) than P25 (S_{BET} = 55 m^2 g^{-1} and V_p = 0.13 cm^3 g^{-1}), which seems to be related with the smaller size of the prepared TiO_2 particles in comparison to P25 (as confirmed by TEM – not shown).

Different tendencies were observed for the composites, depending on the type of carbon material used and the carbon content. The results show that only the GO-TiO_2 composites (S_{BET} = 110 and 200 m^2 g^{-1} and V_p = 0.17 and 0.32 cm^3 g^{-1} respectively for GO-TiO_2-4 and GO-TiO_2-12) presented S_{BET} and V_p comparable to that of TiO_2 (S_{BET} = 120 m^2 g^{-1}; V_p = 0.11

$cm^3\ g^{-1}$). These composites have a higher surface area than GO because aggregation of GO sheets occurs when the suspension of GO is dried to perform N_2 adsorption analysis and, for this reason, the surface area measured for the GO material is lower than its effective surface area in suspension.

The lower values obtained for the composites prepared with CNT (S_{BET} = 49 and 61 $m^2\ g^{-1}$ and V_p = 0.074 and 0.089 $cm^3\ g^{-1}$ respectively for CNT-TiO_2-4 and CNT-TiO_2-12) as well as for C_{60} (S_{BET} = 78 and 82 $m^2\ g^{-1}$ and V_p = 0.10 and 0.11 $cm^3\ g^{-1}$ respectively for C_{60}-TiO_2-4 and C_{60}-TiO_2-12), when compared to TiO_2, may be due to the agglomeration of the TiO_2 particles induced by the presence of the carbon material and by the treatment with nitrogen at 200 ºC during the preparation step of the composites. It is also possible to observe that the change in S_{BET} and V_p is not significant when the carbon content increases from 4 wt.% to 12 wt.% for these composites (less than 12 $m^2\ g^{-1}$ in S_{BET} and 0.02 $cm^3\ g^{-1}$ in V_p). However, in the case of GO-TiO_2 composites a significant development of the porosity (i.e. S_{BET} and V_p) was observed for the same increase in the carbon contents (as high as 93 $m^2\ g^{-1}$ in S_{BET} and 0.15 $cm^3\ g^{-1}$ in V_p). In fact, a larger volume of N_2 adsorbed at high relative pressure and a clear hysteresis loop was observed for GO-TiO_2-12 compared to C_{60}-TiO_2-12 and CNT-TiO_2-12 (Figure 1).

3.1.3. Scanning electron microscopy (SEM) and transmission electron microscopy (TEM)

Figures 2a-j show representative SEM images of the oxidized carbon materials, TiO_2 and all composites. Figures 2a, b and c show the different morphologies of the nanocarbons (CNT, GO and C_{60}, respectively). The CNT sample consists of nanotubes with diameters in a range of 10-20 nm, while the micrograph of the GO material clearly shows the sheets of GO. For the C_{60} sample, some spherical-like particles were observed (as shown in a lower magnification micrograph - Figure 2c, inset) but in general a non-homogeneous structure was

obtained, probably due to the sonication and oxidation treatments performed, and accordingly to what is reported elsewhere [32]. The morphology of TiO_2 consists of spherical-like particles aggregating in clusters of TiO_2 particles (Figure 2d).

The composites presented different morphologies related to the nanocarbons used, the carbon content, the dispersion degree of the carbon material and the accessibility for TiO_2 assembling on GO during the preparation method. In general, materials comprising carbon contents of 4 wt.% (Figures 2e, g and i) showed the corresponding nanocarbon material homogenously decorated with well-dispersed particles of TiO_2. However, the morphologies of the composites prepared with higher content of CNT, C_{60} and GO (12 wt.%, Figures 2f, h and j, respectively), were somewhat different, presenting mostly larger clusters with irregularly dispersed TiO_2 particles, not so pronounced in the case of C_{60}-TiO_2-12 (Figure 2h). Among all composites, the exclusive morphology obtained for GO-TiO_2-4 (Figure 2i) must be underlined, the TiO_2 particles being uniformly assembled on both sides of GO nanosheets. It was also possible to determine by HRTEM (not shown) that the size of TiO_2 crystallites was nearly 5 nm, and by SAED analysis that TiO_2 is present as the anatase crystalline phase.

3.1.4. Temperature programmed desorption (TPD)

The surface chemistry of the materials was modified by introducing oxygenated surface groups (as described in section 2.2), leading to increased acidic properties. In general, the presence of oxygenated groups improves the interaction between the carbon phase and TiO_2 particles by the formation of Ti-O-C bonds [20]. The oxidation treatment with $(NH_4)_2S_2O_8$ carried out over CNT and C_{60} was less effective than the method used for GO, which included stronger oxidation agents such as H_2SO_4 and $KMnO_4$ [23].

The results showed that the oxygen content evolved during TPD experiments (not shown) follows the order: C_{60} (0.91 wt.%) < CNT (1.7 wt.%) < GO (23 wt.%). The high oxygen content detected for the GO sample corresponds to a much larger CO and CO_2 evolution in comparison with the other nanocarbon materials (respectively 3228 and 5387 μmol g^{-1} for GO, 414 and 328 μmol g^{-1} for CNT and 203 and 181 μmol g^{-1} for C_{60}), this evolution observed for GO mainly occurring at low temperatures (180-200 ºC) in contrast with common CO and CO_2 evolution for other carbon materials (220-900 ºC) [28, 29].

The CO and CO_2 evolved from GO in this very narrow range of low temperatures has been ascribed in literature to epoxy and hydroxyl groups located in basal plane sites, which are more labile than the groups located at the edges. Isolated epoxies and hydroxyls are expected to be released only as CO; however, it has been suggested that due to their high density in GO, the release of CO_2 is facilitated [33]. The surface chemistry of GO should be then responsible not only for its high dispersion in the solution during the preparation of the composites, but also for the good assembly of the TiO_2 particles on GO, as observed by SEM (Figure 2i).

3.1.5. Diffuse reflectance UV-Vis spectroscopy

The optical properties of the as-prepared catalysts were determined using the diffuse reflectance (DR) UV-Vis spectra expressed in terms of Kulbelka-Munk equivalent absorption units as shown in Figure 3. The bare TiO_2 prepared by LPD method (TiO_2) showed an intense absorption band in the UV region. The addition of any carbon material (regardless of the amount used) into the TiO_2 raises the baseline absorbance in the visible region leading to a band-gap narrowing. The increase in absorption in the visible region is proportional to the carbon phase. In addition, the absorption was found to depend on the kind of nanocarbon

used for the same carbon content, a higher absorption in the visible region being observed for nanocomposites prepared with GO, then with CNT and finally with C_{60}.

3.2. Photocatalytic experiments

3.2.1. Pollutant adsorption in dark phase

Preliminary experiments under dark conditions were performed to establish the adsorption-desorption equilibrium of the pollutants at room temperature (25 ºC). As shown in Figure 4, the adsorption capacity was around 7%, 4% or 3% of the initial DP concentration for GO-TiO_2-4, CNT-TiO_2-4 and C_{60}-TiO_2-4, respectively, increasing with the nanocarbon content (15%, 7% or 5% for GO-TiO_2-12, CNT-TiO_2-12 and C_{60}-TiO_2-12, respectively). For MO, the highest adsorption capacity was obtained with the materials prepared with GO (8% or 15% for GO-TiO_2-4 and GO-TiO_2-12, respectively) followed by the catalysts synthesized with CNT (4% or 6% for CNT-TiO_2-4 and CNT-TiO_2-12, respectively) and C_{60} (4% or 5% for C_{60}-TiO_2-4 and C_{60}-TiO_2-12, respectively).

At the pH values used for the photocatalytic experiments (natural pH of 5.9 for DP and 4.4 for MO), the model pollutant molecules are mainly protonated in solution while the surface charge of the nanocarbon composites will change depending on the case. For DP adsorption, the surface of GO-TiO_2-4 (pH_{PZC} ≈ 3.0) is negatively charged and electrostatic attractions should be expected between the carbon surface and the DP molecules. The same is valid in the case of the composites prepared with CNT (pH_{PZC} ≈ 5.1) and C_{60} (pH_{PZC} ≈ 5.6). They all have pH_{PZC} below the pH of the medium. In the case of MO adsorption, electrostatic repulsions are expected between protonated MO molecules and the carbon surface for both CNT-TiO_2-4 and C_{60}-TiO_2-4 due to the slightly positively charged catalyst surface.

The porosity of the prepared nanocarbon composites (i.e. as inferred from S_{BET} and V_p) could also affect the different adsorption capacities. The change in S_{BET} and V_p was significant

when the carbon content was increased (Table 1), the highest porosity being observed for the composites prepared with GO (in accordance with the highest adsorption obtained), which significantly differs from the porosity determined for composites prepared with CNT and C_{60}. Therefore, these results indicate that both pH_{PZC} and porosity push on the same direction the observed effect on the adsorption capacity of the nanocarbon composites. Even so, adsorption was always lower than 15% of the initial pollutant concentration, indicating that adsorption in the dark will contribute only to a slight removal of the pollutant during the adsorption-desorption period (i.e. before turning on the lamp).

3.2.2. Photocatalytic degradation of DP

The nanocarbon based-TiO_2 materials obtained with different CNT, C_{60} and GO carbon contents, as well as TiO_2 and P25 materials, were tested in the photodegradation of DP under near-UV/Vis (Figures 5a and b) and visible light (Figures 5c and d) irradiation. The corresponding pseudo-first order rate constants (k) are all collected in Table 2, together with the respective regression coefficient of the model (r^2), in general indicating good fitting of the model to the experimental data.

For experiments performed under near-UV/Vis irradiation (Figures 5a and b) the photolysis of DP leads to ca. 6% DP conversion in 60 min, indicating that DP is a very refractory pollutant in the absence of a catalyst. It is also noticeable that the introduction of any content of nanocarbon material leads to an increase in the efficiency for DP removal in comparison to bare TiO_2. These results suggest a synergistic effect between the carbon phase and TiO_2 particles which depends on the nature and content of a given nanocarbon material.

The photocatalytic activity of the composites prepared with a carbon content of 4 wt.%, TiO_2 and P25 follows the order (Figure 5a): GO-TiO_2-4 (62×10^{-3} min^{-1}) ≈ P25 (56×10^{-3} min^{-1}) > C_{60}-TiO_2-4 (33×10^{-3} min^{-1}) > CNT-TiO_2-4 (24×10^{-3} min^{-1}) > TiO_2 (16.8×10^{-3} min^{-1}) where

the values in brackets refer to the pseudo-first order rate constants (Table 2). Therefore, among the photocatalysts containing 4 wt.% of carbon, the highest photocatalytic performance under near-UV/Vis irradiation was found for the GO composite (GO-TiO_2-4), with comparable efficiency to that of the benchmark P25 catalyst. In our previous study [21] the good performance of GO-TiO_2-4 was attributed to the good TiO_2 distribution in the composite prepared with this GO content, leading to a good assembly and interfacial coupling between the GO sheets and TiO_2 nanoparticles, as can be observed in the SEM micrograph of this composite (Figure 2i), acting as an efficient electron acceptor and donor.

When the GO content is increased to 12 wt.% (Figure 5b) a very pronounced decrease in the photocatalytic activity is observed (from 62×10^{-3} to 18.1×10^{-3} min^{-1}, Table 2) attributed to the very different morphology found for GO-TiO_2-12 (Figure 2j) in comparison to that observed for GO-TiO_2-4 (Figure 2i). The associated mineralization shows a very similar trend (Figure 6); i.e., the results revealed that after 60 min of near-UV/Vis illumination, the composites prepared with GO content of 4 wt.% produced a TOC reduction of 50%, while a GO content of 12 wt.% leads to a mineralization of ca. 20%.

In contrast with GO-TiO_2 composites, the photocatalytic activities of composites prepared with 12 wt.% of CNT (29.3×10^{-3} min^{-1}) and C_{60} (44×10^{-3} min^{-1}) are higher than those obtained with composites prepared with 4 wt.% of carbon phase (Table 2). These results underline the importance of controlling the carbon loading of the composites in order to achieve an optimal synergistic interaction between a given nanocarbon material and TiO_2. In addition, CNT-TiO_2-12 and C_{60}-TiO_2-12 were more efficient for DP degradation under near-UV/Vis illumination than GO-TiO_2-12, C_{60}-TiO_2-12 exhibiting the highest photocatalytic activity among the materials prepared with this higher carbon content (k = 44×10^{-3}, 29.3×10^{-3} or 18.1×10^{-3} min^{-1} for C_{60}-TiO_2-12, CNT-TiO_2-12 and GO-TiO_2-12, respectively).

Therefore, these results indicate that the optimal carbon content found for the composites prepared with GO is not the same as for those prepared with CNT and C_{60}. In fact, carbon contents higher than 4 wt.% (ca. 10-20 wt.%) have been systematically reported in literature as optimal for degradation of several organic pollutants with CNT-TiO_2 composites [4, 10, 34], so that the synergistic effect is induced by a strong interphase interaction between CNT and TiO_2, CNT acting as a photosensitizer rather than as an adsorbent [34]. Concerning C_{60}-TiO_2 composites, the contribution from different C_{60} contents to the specific surface areas is negligible (S_{BET} = 78 or 82 $m^2\ g^{-1}$ for C_{60}-TiO_2-4 and C_{60}-TiO_2-12, respectively) while the photocatalytic activity increased with the carbon content (k = 33×10^{-3} or 44×10^{-3} min^{-1} for C_{60}-TiO_2-4 and C_{60}-TiO_2-12, respectively). These results indicate that the higher activity for C_{60}-TiO_2 composites prepared with higher carbon content is not really associated to the surface area or to the adsorption capacity of these materials (ca. 5%, Figure 4). Thus, the main contribution of C_{60} in these nanocomposites seems to be related to the interfacial charge transfer process that can effectively inhibit electron–hole recombination since it has been reported that the delocalized π electron structure of C_{60} facilitates the transfer of photoinduced electrons and can perform as an excellent electron acceptor under near-UV/Vis illumination [32, 35, 36]. Even so, among all the materials tested in the present work under near-UV/Vis illumination, GO-TiO_2-4 presented the highest photocatalytic efficiency (k = 62×10^{-3} min^{-1}).

The photocatalytic activity of the nanocarbon composites for DP degradation under visible light illumination was also evaluated (Table 2, and Figures 5c and d). As expected, the pseudo-first order rate constants in this case are lower than those obtained under near-UV/Vis irradiation, because the use of the cut-off longpass filter in visible light experiments decreases the photon flux (just selects photons with λ > 430 nm). The activity of the tested materials (Table 2) decreases in the order: GO-TiO_2-4 (3.4×10^{-3} min^{-1}) > CNT-TiO_2-12 (2.7×10^{-3}) >

CNT-TiO_2-4 (1.9×10^{-3} min^{-1}) > C_{60}-TiO_2-4 (1.3×10^{-3} min^{-1}) > GO-TiO_2-12 (1.2×10^{-3} min^{-1}) ~ C_{60}-TiO_2-12 (1.2×10^{-3} min^{-1}) > P25 (1.1×10^{-3} min^{-1}) > TiO_2 (1.0×10^{-3} min^{-1}). Therefore, the results show that the GO composite containing 4 wt.% and the CNT composites with 4 wt.% and 12 wt.% exhibited the highest photocatalytic activities under visible light, in particular when compared with P25 and bare TiO_2.

These results corroborate the role of GO and CNT in extending the photocatalytic activity of TiO_2 under visible light illumination. The high efficiency of GO-TiO_2 and CNT-TiO_2 composites under visible light illumination can be attributed to the role of the carbon phase acting as sensitizer (electron donor). In that case, electrons excited by visible light in localized sp^2 states of the nanocarbon material would be injected into the conduction band of TiO_2, where O_2 molecules can readily trap them and produce the radical species. This effect has been previously reported for GO-TiO_2 [21] and CNT-TiO_2 [4] composites.

It is also of interest to note that no appreciable DP degradation was observed for the composites containing C_{60}, the pseudo-first order rate constants obtained with C_{60}-based composites being quite similar (1.3×10^{-3} or 1.2×10^{-3} min^{-1} for C_{60}-TiO_2-4 and C_{60}-TiO_2-12, respectively) to that obtained with P25 (1.1×10^{-3} min^{-1}). This finding is in line with the results obtained by diffuse reflectance UV-Vis spectroscopy (Figure 3). Only a moderate absorption increase in the visible spectral range was observed for the C_{60}-TiO_2 composites, while a strong increase of light absorption was obtained for the GO-TiO_2 and CNT-TiO_2 composites (proportional to the GO or CNT content into the TiO_2 matrix). These observations are in agreement with previous results reported for C_{60}-TiO_2 composites [35].

Overall, GO-TiO_2-4 presented the highest photocatalytic activity for DP degradation under both near-UV/Vis and visible light irradiation, the pseudo-first order rate constants being 62×10^{-3} min^{-1} or 3.4×10^{-3} min^{-1}, respectively.

3.2.3. Photocatalytic degradation of MO

The photocatalytic activities of the nanocarbon based-TiO_2 materials, P25 and bare TiO_2 were also evaluated for the degradation of MO under near-UV/Vis (Figures 7a and b) and visible light (Figures 7c and d) irradiation, the respective pseudo-first order rate constants being given in Table 2.

Under near-UV/Vis irradiation (Figures 7a and b), once again the results show that there is an increase in the photocatalytic efficiency with the introduction of any nanocarbon material in TiO_2. For the composites with carbon content of 4 wt.%, TiO_2 and P25, the pseudo-first order rate constants under near-UV/Vis irradiation were found as (Table 2): GO-TiO_2-4 (126×10^{-3} min^{-1}) > CNT-TiO_2-4 (75×10^{-3} min^{-1}) > P25 (52×10^{-3} min^{-1}) > C_{60}-TiO_2-4 (25.3×10^{-3} min^{-1}) > TiO_2 (7.2×10^{-3} min^{-1}). GO-TiO_2-4 presented not only a higher photocatalytic activity but also a higher TOC reduction in comparison to all other materials (Figure 6). Therefore, GO-TiO_2 and CNT-TiO_2 composites comprising 4 wt.% of carbon exhibited higher photocatalytic activity than P25 for MO degradation. The same trend was also observed under visible light illumination (Figures 7c and d), GO-TiO_2-4 and CNT-TiO_2-4 revealing to be more efficient than P25 and TiO_2 for degradation of MO (k =7.7×10^{-3}, 4.4×10^{-3}, 1.3×10^{-3} or 1.0×10^{-3} min^{-1} for GO-TiO_2-4, CNT-TiO_2-4, P25 and TiO_2, respectively).

For the 12 wt.% of carbon content composites, a very pronounced decrease in activity was observed (k = 33.3×10^{-3}, 12×10^{-3} or 11×10^{-3} min^{-1} for CNT-TiO_2-12, C_{60}-TiO_2-12 and GO-TiO_2-12, respectively). The different photocatalytic efficiencies obtained over the tested composites for MO degradation in comparison with the results obtained for DP may indicate a dependence of the photocatalytic activity with the kind of target pollutant studied. In fact, the photocatalytic mechanism for DP mediated by holes is more important than the mechanism mediated by photoexcited electrons, while a photoreduction mechanism is mainly observed for MO, involving photogenerated electrons, as recently reported [22].

Therefore, globally speaking, the obtained results indicate that the highest DP and MO degradation rates under both near-UV/Vis and visible light irradiation were found for the composite comprising 4 wt.% of GO, which should be related to the easily accessible 2D structure of GO containing abundant functional oxygen groups on the basal plane (as concluded from TPD analysis in section 3.1.4) which are beneficial for driving an ideal distribution of TiO_2 on GO. For this reason, this material was selected for the subsequent experiments.

3.2.4. GO-TiO_2 into hollow fibres for technological photocatalytic applications

The use of photocatalysts in powder form has been associated with many drawbacks including the difficult separation of the catalyst from the treated effluent, thus increasing the capital and operation costs. For this reason, GO-TiO_2-4 (the most active nanostructured photocatalyst) was immobilized into the matrix of alginate porous hollow fibres (the resulting material hereafter labelled as GO-TiO_2-4/APHF) and its efficiency was evaluated under near-UV/Vis irradiation in continuous mode experiments.

SEM micrographs of GO-TiO_2-4/APHF are shown in Figure 8. Their internal diameter reaches 500 μm and their wall thickness is around 41 μm. The external surface exhibits high roughness with GO-TiO_2 in random orientation.

Regarding the photocatalytic experiment, before turning on the lamp for the first time, a long dark phase (up to 24 hours) allowed the saturation of the fibre with the pollutant. After the lamp was turned on, a DP conversion of more than 70% was obtained. This performance was kept after several dark/bright cycles, as shown in Figure 9.

As mentioned previously (Figures 5 and 7), powdered GO-TiO_2-4 proved to be an excellent material in the photocatalytic degradation of MO and somewhat less effective, but still very efficient in DP photocatalytic degradation. However, when incorporated in the hollow fibres

this trend was reversed, as the composite material showed very poor performance for MO degradation (data not shown). In both cases the photocatalytic conversion was diminished due to the immobilization, this showing that the contribution of direct photocatalytic oxidation of the adsorbed pollutants is one of the important mechanistic pathways. The low MO conversion can be attributed to the low affinity of this molecule to alginate. Indeed adsorption capacity of the composite fibres after 30 min in the dark for MO and DP was found to reach 4% or 16%, respectively, and maintained afterwards.

Electrostatic interactions have long been established as the mechanism of sorption on alginate, the main constituent of the hollow fibres. Alginate, an anionic polysaccharide, interacts favourably with a cationic molecule such as DP and less favourable with MO. The poor affinity for MO is probably the main cause for the poor performance of GO-TiO_2-4/APHF in the MO photocatalytic degradation. Poor adsorption capacity and slow diffusion result in reduced photocatalytic site accessibility and lower conversion efficiency. On the other hand, the high affinity of alginate for DP results in faster diffusion through the polymeric matrix rendering the photocatalytic GO-TiO_2 nanoparticles more accessible.

Apart from the high activity in consecutive light-dark cycles, the fibres also exhibit high stability. Even so, possible degradation of the polymer containing the photocatalyst may occur during the experiment because a peculiar peak in absorbance, with maxima at 204 and 238 nm was observed in the HPLC chromatograms of liquid samples (this peak was not observed in experiments without fibres). This should be better investigated in future works as the effect on both photocatalytic activity and stability could be negative, if the fibres are disintegrated when exposed to very long periods of irradiation; on the other hand, it could also be positive if the applied irradiation just activates the fibres by allowing better accessibility of the pollutant molecules to the photocatalyst without significant damage of the

fibres. In the latter case it would be more appropriate to activate the fibres during their preparation.

Anyway, the results are very promising in terms of productivity (Figure 9b), as the (DP removed):(DP fed) ratio reached the same value for all three consecutive cycles performed in continuous mode. Additional work is required to validate the possible use of such composite photocatalytic fibres in practical technological applications (e.g. water purification devices) [25, 37] as well as their optimisation in terms of catalyst content, porous properties and other important parameters.

4. Conclusions

Nanocarbon-TiO_2 composites using different carbonaceous materials (GO and oxidized CNT and C_{60}) with different weight ratios were used in the photocatalytic degradation of DP pharmaceutical compound and MO dye. High oxygen content and a large CO and CO_2 evolution were detected for GO in comparison to the other nanocarbon materials that were studied. The results suggest a synergistic effect between the carbon phase and TiO_2 particles.

The improvement on the efficiency of the photocatalytic process depends on the nature and content of the nanocarbon used. Among all the prepared composites, GO-TiO_2 comprising 4 wt.% of GO (GOT-TiO_2-4) exhibited the highest photocatalytic activity under near-UV/Vis and visible light irradiation (exceeding that of P25 and bare TiO_2 photocatalysts), which was attributed to the optimal self-assembly between GO and TiO_2 particles and acting as electron acceptor and donor, this material having the additional advantage that it can be produced at affordable costs in comparison with CNT-TiO_2 and C_{60}-TiO_2 composites.

The most active photocatalyst (GO-TiO_2-4) was immobilized into alginate hollow fibres, presenting considerably high activity and stability in consecutive light-dark cycles of continuous reaction operation and, therefore, showing promising results for future

technological applications. Even so, further systematic experiments are still needed in order to better access the activity and stability of the prepared photocatalytic fibres.

Acknowledgements

Financial support for this work was provided by projects PTDC/AAC-AMB/122312/2010 and PEst-C/EQB/LA0020/2011 financed by FEDER through COMPETE and by FCT - Fundação para a Ciência e a Tecnologia, and by the European Commission (Clean Water - Grant Agreement nº 227017). SMT and LMPM acknowledge financial support from SFRH/BPD/74239/2010 and SFRH/BPD/88964/2012.

References

[1] R. Leary, A. Westwood, Carbon 49 (2011) 741-772.

[2] A. Di Paola, E. García-López, G. Marcì, L. Palmisano, Journal of Hazardous Materials 211–212 (2012) 3-29.

[3] S. Morales-Torres, L.M. Pastrana-Martínez, J.L. Figueiredo, J.L. Faria, A.M.T. Silva, Environ. Sci. Pollut. Res. 19 (2012) 3676-3687.

[4] W. Wang, P. Serp, P. Kalck, C.G. Silva, J.L. Faria, Materials Research Bulletin 43 (2008) 958-967.

[5] J. Sun, L. Gao, Carbon 41 (2003) 1063-1068.

[6] Y. Yao, G. Li, S. Ciston, R.M. Lueptow, K.A. Gray, Environmental Science & Technology 42 (2008) 4952-4957.

[7] C.G. Silva, J.L. Faria, ChemSusChem 3 (2010) 609-618.

[8] C.G. Silva, J.L. Faria, Applied Catalysis B: Environmental 101 (2010) 81-89.

[9] B. Gao, G.Z. Chen, G. Li Puma, Applied Catalysis B: Environmental 89 (2009) 503-509.

[10] M.J. Sampaio, C.G. Silva, R.R.N. Marques, A.M.T. Silva, J.L. Faria, Catalysis Today 161 (2011) 91-96.

[11] F.-J.Z. Won-Chun Oh, Chang Sung Lim, Ming-Liang Chen, Journal of Ceramic Processing Research 11 (2010) 479-484.

[12] I. Ji Hyuk, Y. Seung Jae, Y. Chang Hun, P. Chong Rae, Nanotechnology 23 (2012) 035604.

[13] S. Mu, Y. Long, S.-Z. Kang, J. Mu, Catalysis Communications 11 (2010) 741-744.

[14] Y. Long, Y. Lu, Y. Huang, Y. Peng, Y. Lu, S.-Z. Kang, J. Mu, The Journal of Physical Chemistry C 113 (2009) 13899-13905.

[15] J. Lin, R. Zong, M. Zhou, Y. Zhu, Applied Catalysis B: Environmental 89 (2009) 425-431.

[16] V. Krishna, N. Noguchi, B. Koopman, B. Moudgil, Journal of Colloid and Interface Science 304 (2006) 166-171.

[17] V. Krishna, D. Yanes, W. Imaram, A. Angerhofer, B. Koopman, B. Moudgil, Applied Catalysis B: Environmental 79 (2008) 376-381.

[18] H. Zhang, X. Lv, Y. Li, Y. Wang, J. Li, ACS Nano 4 (2009) 380-386.

[19] O. Akhavan, E. Ghaderi, The Journal of Physical Chemistry C 113 (2009) 20214-20220.

[20] S. Morales-Torres, L.M. Pastrana-Martínez, J.L. Figueiredo, J.L. Faria, A.M.T. Silva, Applied Surface Science (2013) in press, doi: 10.1016/j.apsusc.2012.1011.1157.

[21] L.M. Pastrana-Martínez, S. Morales-Torres, V. Likodimos, J.L. Figueiredo, J.L. Faria, P. Falaras, A.M.T. Silva, Applied Catalysis B: Environmental 123–124 (2012) 241-256.

[22] L.M. Pastrana-Martínez, S. Morales-Torres, A.G. Kontos, N.G. Moustakas, J.M. Doña-Rodríguez, J.L. Faria, P. Falaras, A.M.T. Silva, Chemical Engineering Journal (2013) in press, doi: 10.1016/j.cej.2012.1011.1040

[23] W.S. Hummers, R.E. Offeman, Journal of the American Chemical Society 80 (1958) 1339-1339.

[24] C. Moreno-Castilla, M.A. Ferro-Garcia, J.P. Joly, I. Bautista-Toledo, F. Carrasco-Marin, J. Rivera-Utrilla, Langmuir 11 (1995) 4386-4392.

[25] S.K. Papageorgiou, F.K. Katsaros, E.P. Favvas, G.E. Romanos, C.P. Athanasekou, K.G. Beltsios, O.I. Tzialla, P. Falaras, Water Research 46 (2012) 1858-1872.

[26] S. Brunauer, P.H. Emmett, E. Teller, Journal of the American Chemical Society 60 (1938) 309-319.

[27] J.R. F. Rouquerol, K. Sing, Adsorption by Powders and Porous Solids, Academic Press, London, 1999.

[28] J.L. Figueiredo, M.F.R. Pereira, M.M.A. Freitas, J.J.M. Órfão, Carbon 37 (1999) 1379-1389.

[29] J.L. Figueiredo, M.F.R. Pereira, M.M.A. Freitas, J.J.M. Órfão, Industrial & Engineering Chemistry Research 46 (2007) 4110-4115.

[30] M.A. Ferro-García, J. Rivera-Utrilla, I. Bautista-Toledo, C. Moreno-Castilla, Langmuir 14 (1998) 1880-1886.

[31] G. Newcombe, R. Hayes, M. Drikas, Colloids and Surfaces A: Physicochemical and Engineering Aspects 78 (1993) 65-71.

[32] W.-C. Oh, W.-B. Ko, Journal of Industrial and Engineering Chemistry 15 (2009) 791-797.

[33] P. Solís-Fernández, R. Rozada, J.I. Paredes, S. Villar-Rodil, M.J. Fernández-Merino, L. Guardia, A. Martínez-Alonso, J.M.D. Tascón, Journal of Alloys and Compounds 536S (2012) S532-537.

[34] W. Wang, P. Serp, P. Kalck, J.L. Faria, Applied Catalysis B: Environmental 56 (2005) 305-312.

[35] V. Apostolopoulou, J. Vakros, C. Kordulis, A. Lycourghiotis, Colloids and Surfaces A: Physicochemical and Engineering Aspects 349 (2009) 189-194.

[36] J. Yu, T. Ma, S. Liu, Physical Chemistry Chemical Physics 13 (2011) 3491-3501.

[37] C.P. Athanasekou, G.E. Romanos, F.K. Katsaros, K. Kordatos, V. Likodimos, P. Falaras, Journal of Membrane Science 392–393 (2012) 192-203.

Table 1. BET surface area (S_{BET}) and total pore volume (V_p) of the synthesized materials.

Sample	$S_{BET}/(m^2\ g^{-1})$	$V_p/(cm^3\ g^{-1})$
GO	21	0.0027
CNT	110	0.26
C_{60}	n.d.	n.d.
P25	55	0.13
TiO_2	120	0.11
C_{60}-TiO_2-4	78	0.10
C_{60}-TiO_2-12	82	0.11
CNT-TiO_2-4	49	0.074
CNT-TiO_2-12	61	0.089
GO-TiO_2-4	110	0.17
GO-TiO_2-12	200	0.32

Table 2. Pseudo first-order kinetic rate constant (k) and regression coefficient (r^2) of DP and MO degradation under near-UV/Vis and visible irradiation with different photocatalysts.

	Diphenhydramine (DP)				Methyl orange (MO)			
	near-UV/Vis		Visible		near-UV/Vis		Visible	
	k (10^{-3} min^{-1})	r^2	k (10^{-3} min^{-1})	r^2	k (10^{-3} min^{-1})	r^2	k (10^{-3} min^{-1})	r^2
GO-TiO_2-4	62 ± 3	0.998	3.4 ± 0.2	0.99	126 ± 9	0.99	7.7 ± 0.5	0.99
CNT-TiO_2-4	24 ± 2	0.992	1.9 ± 0.3	0.98	75 ± 1	0.999	4.4 ± 0.7	0.94
C_{60}-TiO_2-4	33 ± 4	0.98	1.3 ± 0.2	0.98	25.3 ± 0.3	0.999	1.4 ± 0.2	0.95
GO-TiO_2-12	18.1 ± 0.5	0.9998	1.2 ± 0.2	0.998	11 ± 1	0.97	1.4 ± 0.2	0.96
CNT-TiO_2-12	29.3 ± 0.8	0.998	2.7 ± 0.5	0.96	33.3 ± 0.9	0.998	2.7 ± 0.5	0.99
C_{60}-TiO_2-12	44 ± 2	0.997	1.2 ± 0.2	0.93	12 ± 2	0.96	1.3 ± 0.2	0.95
TiO_2	16.8 ± 0.5	0.997	1.0 ± 0.2	0.99	7.2 ± 0.5	0.99	1.0 ± 0.3	0.98
P25	56 ± 4	0.998	1.1 ± 0.1	0.9	52 ± 5	0.99	1.3 ± 0.2	0.9
Photolysis	1.00 ± 0.07	0.9	0.96 ± 0.06	0.99	1.00 ± 0.20	0.9	0.95 ± 0.21	0.9

FIGURE CAPTION

Figure 1. N_2 adsorption–desorption isotherms at −196 ºC for TiO_2 and for the prepared nanocarbon-TiO_2 composites with 12 wt.% of carbon content (from left to right: TiO_2, CNT-TiO_2-12, C_{60}-TiO_2-12 and GO-TiO_2-12).

Figure 2. SEM micrographs for (a) CNT, (b) GO, (c) C_{60}, (d) TiO_2, (e) CNT-TiO_2-4, (f) CNT-TiO_2-12, (g) C_{60}-TiO_2-4, (h) C_{60}-TiO_2-12, (i) GO-TiO_2-4 and (j) GO-TiO_2-12.

Figure 3. Diffuse reflectance UV-Vis spectra of TiO_2 and nanocarbon-TiO_2 composites.

Figure 4. Adsorption capacity of DP and MO for all nanocarbon-TiO_2 composites in the dark phase for 30 min.

Figure 5. Photocatalytic degradation of DP under (a, b) near-UV/Vis and (c, d) visible light illumination over P25, TiO_2 and nanocarbon-TiO_2 composites prepared with (a, c) 4 wt.% and (b, d) 12 wt.% of carbon content (d inset: chemical structure of diphenhydramine).

Figure 6. Total organic carbon (TOC) reduction for DP and MO photodegradation under near-UV/Vis irradiation for TiO_2, P25 and different nanocarbon-TiO_2 composites.

Figure 7. Photocatalytic degradation of MO under (a-b) near-UV/Vis and (c-d) visible light illumination over P25, TiO_2 and nanocarbon-TiO_2 composites (d inset: chemical structure of methyl orange).

Figure 8. SEM micrographs at different magnifications of the GO-TiO_2-4 composite immobilized into alginate porous hollow fibres (GO-TiO_2-4/APHF): (a) wall thickness, (b) external surface.

Figure 9. Photocatalytic degradation of DP over GO-TiO_2-4/APHF in continuous mode under near-UV/Vis irradiation and (b) amount of DP removed as a function of the total DP fed to the reactor.

FIGURE 1

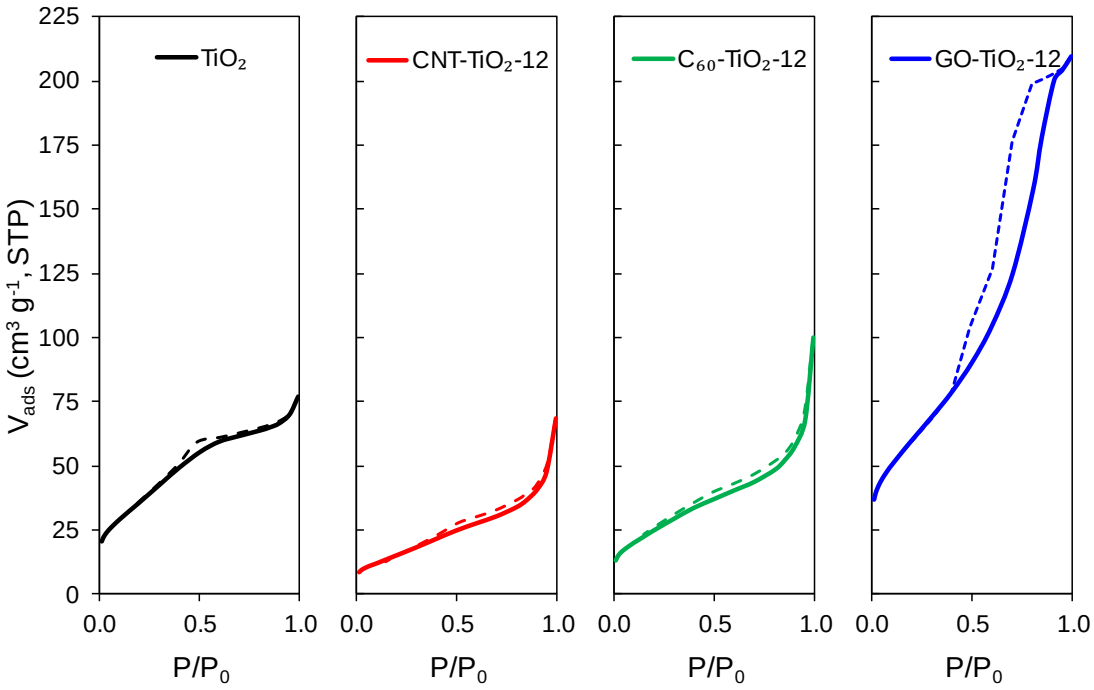
TiO2
CNT-TiO2-12
C60-TiO2-12
GO-TiO2-12
Vads (cm3 g-1, STP)
P/P0
0
25
50
75
100
125
150
175
200
225
0.0
0.5
1.0

FIGURE 2

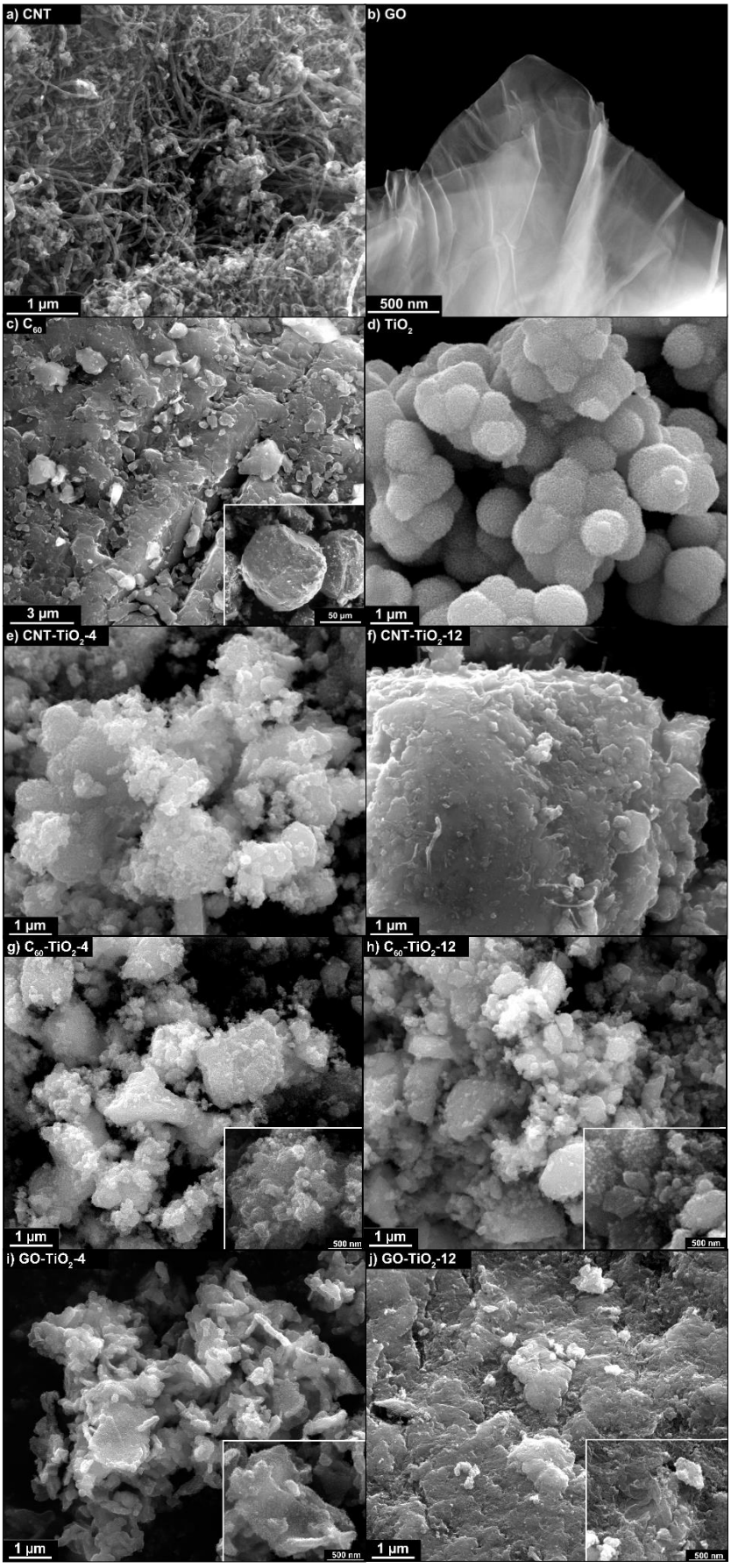
a) CNT
1 µm
b) GO
500 nm
c) C_{60}
3 µm
50 µm
d) TiO_2
1 µm
e) CNT-TiO_2-4
1 µm
f) CNT-TiO_2-12
1 µm
g) C_{60}-TiO_2-4
1 µm
500 nm
h) C_{60}-TiO_2-12
1 µm
500 nm
i) GO-TiO_2-4
1 µm
500 nm
j) GO-TiO_2-12
1 µm
500 nm

FIGURE 3

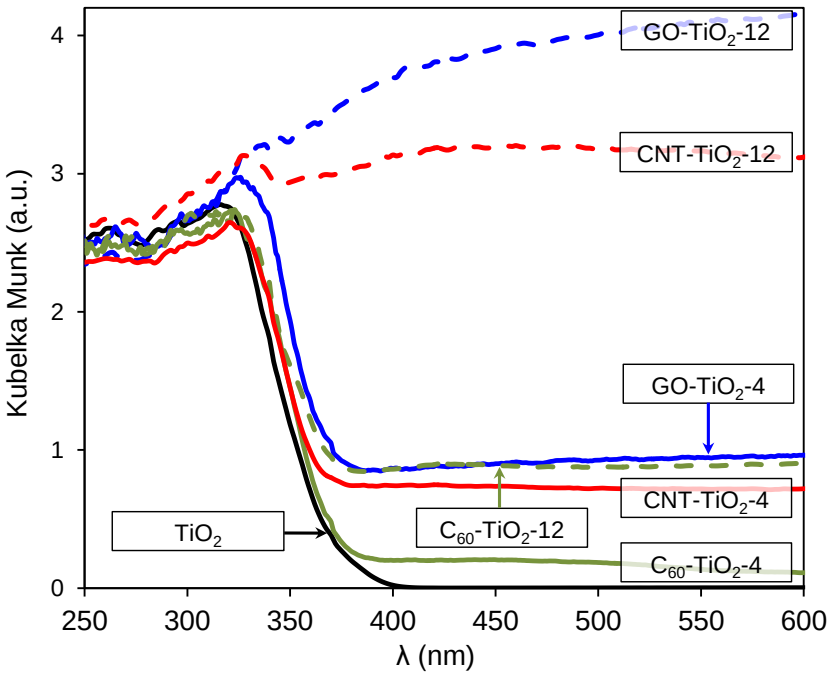
Kubelka Munk (a.u.)
λ (nm)
GO-TiO2-12
CNT-TiO2-12
GO-TiO2-4
CNT-TiO2-4
C60-TiO2-12
C60-TiO2-4
TiO2

FIGURE 4

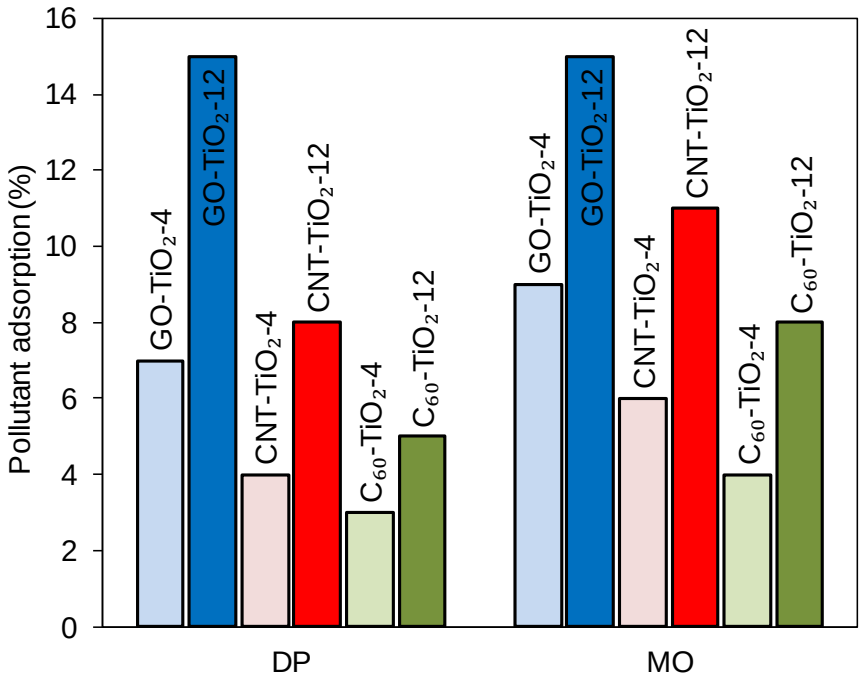
Pollutant adsorption (%)
16
14
12
10
8
6
4
2
0
GO-TiO2-4
GO-TiO2-12
CNT-TiO2-4
CNT-TiO2-12
C60-TiO2-4
C60-TiO2-12
DP
MO

FIGURE 5

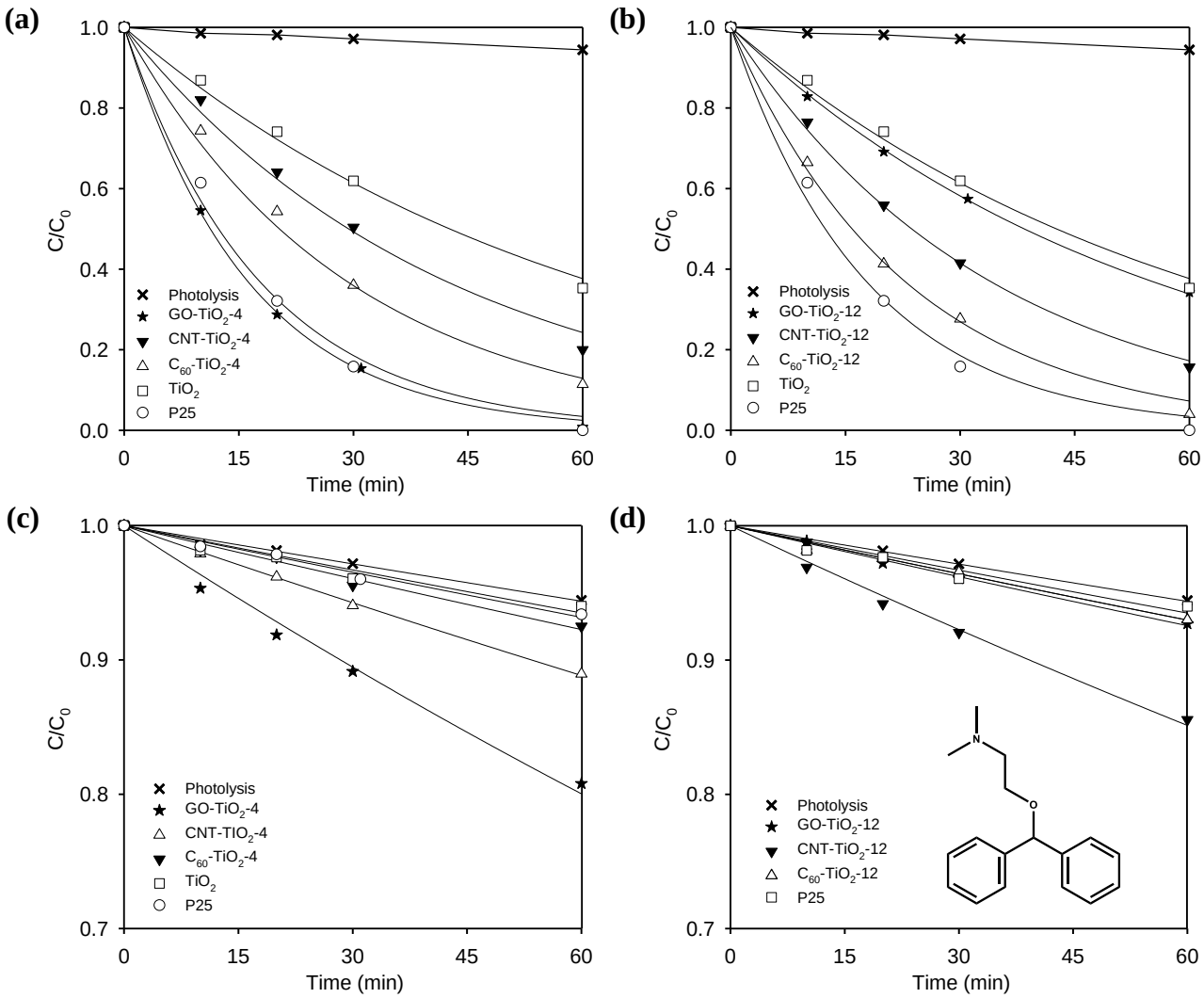
(a)
(b)
(c)
(d)
C/C0
Time (min)
Photolysis
GO-TiO2-4
CNT-TiO2-4
C60-TiO2-4
TiO2
P25
GO-TiO2-12
CNT-TiO2-12
C60-TiO2-12
N
O

FIGURE 6

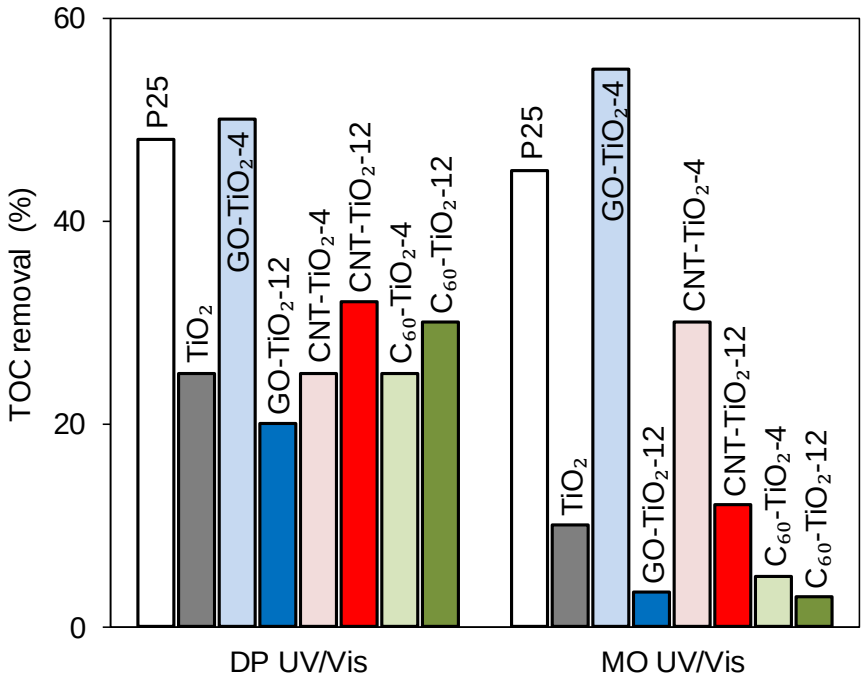
60
40
20
0
TOC removal (%)
P25
TiO2
GO-TiO2-4
GO-TiO2-12
CNT-TiO2-4
CNT-TiO2-12
C60-TiO2-4
C60-TiO2-12
DP UV/Vis
MO UV/Vis

FIGURE 7

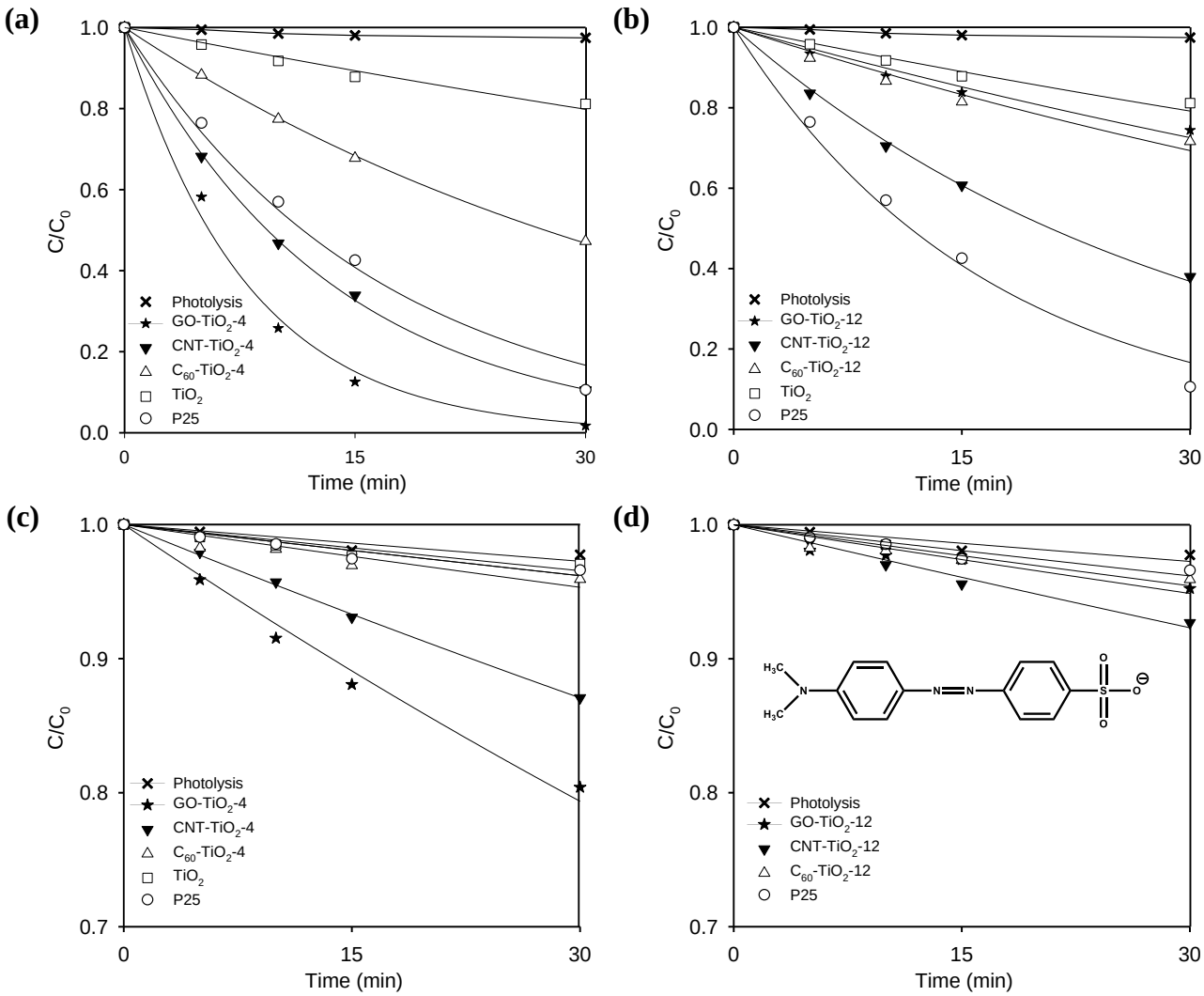
(a)
(b)
(c)
(d)
C/C0
Time (min)
Photolysis
GO-TiO2-4
CNT-TiO2-4
C60-TiO2-4
TiO2
P25
GO-TiO2-12
CNT-TiO2-12
C60-TiO2-12

FIGURE 8

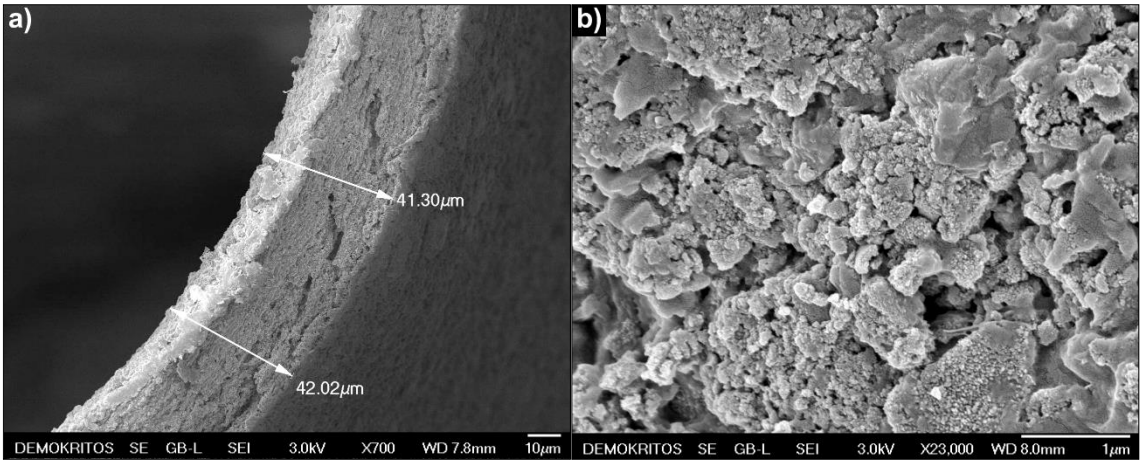
a)
41.30μm
42.02μm
DEMOKRITOS SE GB-L SEI 3.0kV X700 WD 7.8mm 10μm
b)
DEMOKRITOS SE GB-L SEI 3.0kV X23,000 WD 8.0mm 1μm

FIGURE 9

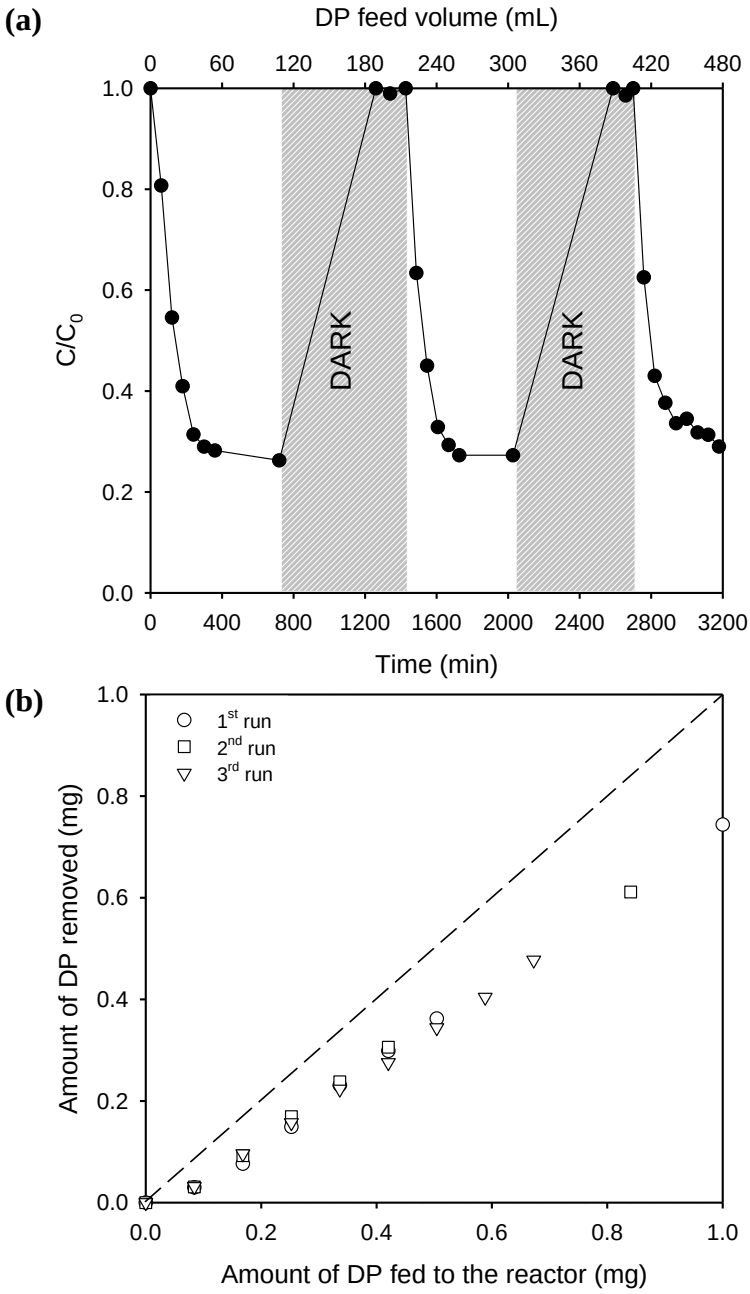
(a)
DP feed volume (mL)
0
60
120
180
240
300
360
420
480
1.0
0.8
0.6
0.4
0.2
0.0
C/C0
DARK
DARK
0
400
800
1200
1600
2000
2400
2800
3200
Time (min)
(b)
1st run
2nd run
3rd run
Amount of DP removed (mg)
0.0
0.2
0.4
0.6
0.8
1.0
Amount of DP fed to the reactor (mg)